

Reversible calcium alloying enables a practical room-temperature rechargeable calcium-ion battery with a high discharge voltage

Meng Wang¹, Chunlei Jiang¹, Songquan Zhang¹, Xiaohe Song¹, Yongbing Tang¹^{*} and Hui-Ming Cheng^{2,3*}

Calcium-ion batteries (CIBs) are attractive candidates for energy storage because Ca^{2+} has low polarization and a reduction potential (-2.87 V versus standard hydrogen electrode, SHE) close to that of Li^+ (-3.04 V versus SHE), promising a wide voltage window for a full battery. However, their development is limited by difficulties such as the lack of proper cathode/anode materials for reversible Ca^{2+} intercalation/de-intercalation, low working voltages ($<2\text{ V}$), low cycling stability, and especially poor room-temperature performance. Here, we report a CIB that can work stably at room temperature in a new cell configuration using graphite as the cathode and tin foils as the anode as well as the current collector. This CIB operates on a highly reversible electrochemical reaction that combines hexafluorophosphate intercalation/de-intercalation at the cathode and a Ca-involved alloying/de-alloying reaction at the anode. An optimized CIB exhibits a working voltage of up to 4.45 V with capacity retention of 95% after 350 cycles.

Developing multivalent ion-based rechargeable batteries would open up new opportunities for high-energy-density storage systems, because one mole of multivalent ions can provide double (for M^{2+}) or triple (for M^{3+}) the number of electrons than in lithium-ion batteries (LIBs)^{1–4}. Among the multivalent cations, Mg^{2+} , Al^{3+} and Ca^{2+} are the most promising candidates because of their stable valence states, small ionic radii, low plating potentials and abundance. Many studies have therefore been carried out on the development of Mg^{2+} - and Al^{3+} -based rechargeable batteries^{1,4}. Although the standard reduction potential of elemental calcium is only 170 mV above that of lithium (500 mV lower than Mg/Mg^{2+} and 1.2 V lower than Al/Al^{3+})^{5–8}, which enables it to have a higher working potential than Mg^{2+} - and Al^{3+} -based batteries, research progress for Ca-ion batteries (CIBs) is far from satisfactory. A previous investigation revealed that, unlike Li^+ ions, Ca^{2+} deposition is impossible because Ca^{2+} ions are difficult to transport through the surface passivation film when a Ca metal electrode is used in organic electrolytes⁹.

Using a molten mixture of CaCl_2 and LiCl as the electrolyte, a molten Ca–Mg alloy and Bi as anode and cathode, respectively, a Ca-based liquid battery has been reported that exhibits a good cycling life at high temperatures ($550\text{--}700^\circ\text{C}$), in spite of its low working voltage ($<1\text{ V}$)¹⁰. Recently, although no redox processes were detected at room temperature, + Ca electrodeposition was observed at $75\text{--}100^\circ\text{C}$ in carbonate electrolytes containing $\text{Ca}(\text{BF}_4)_2$ salt, with a cycling stability assessed for more than 30 cycles to confirm the reversible operation of the Ca metal anode at 100°C (ref. ²). This reversible charge–discharge reaction drew attention to the development of CIBs; however, it is obvious that the working temperature must be decreased to match mainstream application conditions because most portable electronic devices and vehicles operate near room temperature. Moreover, compared to other electrochemical

energy storage systems^{11–14}, the development of CIBs is at an initial stage, and their reported electrochemical performances^{2,9,10} (for example, cycling stability, rate performance and especially working voltage) have remained far from practical requirements. Here, we report a rechargeable Ca-ion battery obtained with a new configuration that provides a highly reversible electrochemical reaction in conventional carbonate solvents at room temperature.

Results and discussion

The configuration and working mechanism of this CIB are presented in Fig. 1a. Graphite was used as the cathode material, and a metal foil that could form an alloy with Ca according to the binary phase diagram was used as both current collector and anode. On charging, PF_6^- anions in the electrolyte (coming from $\text{Ca}(\text{PF}_6)_2$ salt) intercalate the graphite cathode, while Ca ions simultaneously deposit on and react with the metal anode (for example, Zn, Na and Sn). In the discharge process, PF_6^- anions and Ca^{2+} cations, respectively, de-intercalate and de-alloy from the graphite cathode and metal anode, and diffuse back into the electrolyte. The feasibility of reversibly alloying/de-alloying Ca with different metals was assessed to choose a suitable anode for CIBs with good performance (Supplementary Fig. 1). The negligible charge/discharge capacity of the Zn anode indicated its limited reversibility, and, although the discharge capacities of Li and Na anodes are also low, a highly reversible electrochemical reaction was observed with a Sn anode. This CIB (Sn | electrolyte | graphite) features high charge and discharge voltages (Fig. 1b). During charging, three plateaux ($4.21\text{--}4.75$, $4.75\text{--}4.81$ and $4.81\text{--}4.95\text{ V}$) are present in the voltage profile, corresponding to the intercalated phase transformations of graphite during anion intercalation¹⁵. For the discharge process, the de-intercalation of anions from graphite similarly led to another three flat regions ($4.95\text{--}4.47$, $4.47\text{--}4.11$ and $4.11\text{--}3.52\text{ V}$) in the voltage profile, yielding a high

¹Functional Thin Films Research Center, Shenzhen Institutes of Advanced Technology, Chinese Academy of Sciences, Shenzhen, China. ²Tsinghua-Berkeley Shenzhen Institute, Tsinghua University, Shenzhen, China. ³Shenyang National Laboratory for Materials Science, Institute of Metal Research, Chinese Academy of Sciences, Shenyang, China. *e-mail: tangyb@siat.ac.cn; hmceng@sz.tsinghua.edu.cn

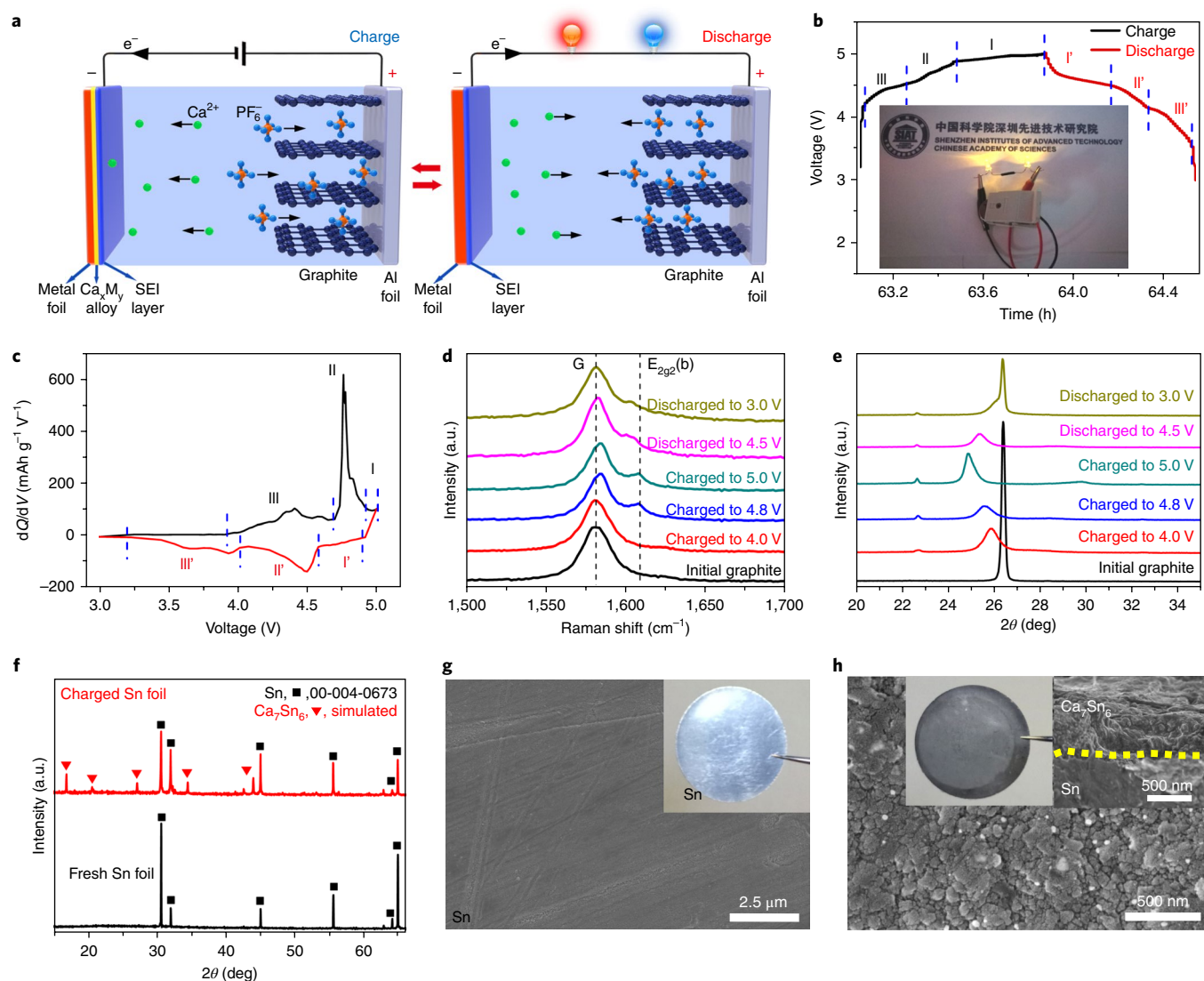


Fig. 1 | Configuration and reaction mechanism of a CIB. **a**, Work schematics of the proposed CIB. Graphite was used as the cathode material for hexafluorophosphate intercalation/de-intercalation, and a metal foil that could form an alloy with Ca was used as both current collector and anode. Green, blue and orange balls represent Ca, F and P atoms, respectively. **b**, Galvanostatic charge-discharge curve of a CIB. Inset: One CIB coin-cell lighting two yellow LEDs in series. **c**, Corresponding dQ/dV curve of the charge-discharge profile in **b**. I, II, III, I', II' and III' in **b** and **c** indicate the different charge and discharge plateaux. **d,e**, Raman (**d**) and X-Ray diffraction (XRD) (**e**) spectra of the graphite cathode at different charged states. **f**, XRD patterns of a fresh and charged Sn anode (after 300 cycles). **g,h**, SEM images of Sn foil anode before battery reaction (**g**) and after 300 cycles (**h**). Dashed yellow line (**h**) shows the interface between Sn and Ca₇Sn₆.

discharge voltage (up to 4.45 V) that is much higher than most values reported for LIBs. This high discharge voltage enables the battery to easily light two yellow light-emitting diodes (LEDs) in series (Fig. 1b, inset). Figure 1c shows the differential capacity profiles, clearly indicating the different states of the battery due to PF₆⁻ intercalation/de-intercalation¹⁵. Correspondingly, three de-intercalation peaks were also observed for the discharge process but with a downward potential shift of 0.1–0.4 V compared to the charging process due to voltage hysteresis¹⁶.

Given the ideal properties of conventional polar aprotic solvents, such as their ability to dissolve salts, their stability, low viscosity and wide utilization in LIBs¹⁷, we investigated their possible use in the CIB system. We first investigated binary electrolyte solvent systems containing one type of cyclic carbonate (propylene carbonate (PC) or ethylene carbonate (EC)), with a high dielectric constant (ϵ) to dissolve a certain amount of salt, and a linear carbonate (ethyl

methyl carbonate (EMC) or dimethyl carbonate (DMC)), featuring low viscosity for high ionic conductivity. Charge-discharge profiles of CIBs with different electrolyte formulations containing 0.8 M Ca(PF₆)₂ are shown in Supplementary Fig. 2a–d. It was found that each solvent plays a specific role in determining the electrochemical performance of the CIB. Electrolytes containing EMC show higher capacities than those with DMC, as was observed in previous studies in which alloyed metal anodes were used¹⁸. EC helps to achieve a relatively high coulombic efficiency, which is consistent with the conclusion that EC can form a protective film on anode materials that prevents continuous electrolyte decomposition¹⁷. The addition of DMC lowered the charge voltage plateaux, suggesting improved reaction kinetics. This phenomenon is consistent with the observation that the addition of DMC gives the electrolyte a lower viscosity and a higher ionic conductivity than other linear carbonates such as EMC and diethyl carbonate (DEC)¹⁹. This effect is favourable

for the diffusion and migration of solvated PF_6^- and Ca^{2+} and thus for improved reaction kinetics. Although CIBs using PC as one of the solvents demonstrated lower coulombic efficiencies because of the poor stability of PC on highly reduced anode surfaces¹⁷, they showed less fluctuation in the discharge capacities. The specific function of these solvents was further verified by controlled experiments using ternary solvent systems (Supplementary Fig. 2e–h), and an ideal electrolyte was achieved by combining all four solvents (EC, PC, DMC and EMC) (vol/vol/vol/vol = 2:2:3:3) containing 0.8 M $\text{Ca}(\text{PF}_6)_2$ (Supplementary Fig. 2i,j). To verify the electrolyte stability in the range of 3.0–5.0 V, we charged a CIB to a higher cutoff potential than 5.0 V (Supplementary Fig. 3). It was found that obvious electrolyte decomposition took place in the region above 5.2 V for the Sn | electrolyte | graphite CIB.

To better understand the working mechanisms of the CIB, we conducted experiments to verify the phase transformation of the anode and cathode. Raman and X-ray diffraction (XRD) measurements confirmed hexafluorophosphate anion intercalation/de-intercalation into/from the graphite cathode during the first cycle (Fig. 1d,e). Only one peak at $1,584\text{ cm}^{-1}$, belonging to the G band of graphite, was observed in the Raman spectra for the initial graphite²⁰. As the battery gradually charged, a new peak at $1,608\text{ cm}^{-1}$ ($E_{2g2}(\text{b})$) characteristic of the boundary layer emerged, which was due to a stage-2 like structure (two graphite layers lie between intercalant layers)²⁰. The intensity increase of this mode during charging indicates the gradual intercalation of hexafluorophosphate anions into the graphite cathode. Full discharge resulted in the recovery of the graphite phase but with a broad shoulder, probably caused by irreversible phase changes of graphite caused by anion intercalation/de-intercalation¹. This phenomenon was further verified by XRD analysis. When the charge voltage gradually increased from 4.0 to 5.0 V, the (002) graphite diffraction peak gradually shifted to lower angles and a new peak was observed at around 22.69° , suggesting the successful intercalation of PF_6^- (ref. 20). During discharge, this shift was gradually reversed (Fig. 1e) because of the PF_6^- de-intercalation.

Figure 1f shows the XRD patterns of a Sn anode at initial and fully charged states. Initially, only diffraction peaks belonging to tetragonal Sn (JCPDS # 00-004-0673) were observed. At the fully charged state after 300 cycles, new peaks arose at 17.09° , 18.31° , 20.75° , 27.29° , 34.45° , 41.30° , 42.52° and 43.89° , and these could be attributed to specific diffraction peaks of Ca_7Sn_6 (this phase was simulated according to the Materials Project²¹). To the best of our knowledge, this is the first report of the preparation of Ca_7Sn_6 alloy, especially by a reversible electrochemical reaction. X-ray photoelectron spectroscopy (XPS) measurements were performed on a charged Sn anode (Supplementary Fig. 4). In the C 1s spectra (Supplementary Fig. 4a), peaks at ~ 284.8 , 286.5 and 289.3 eV corresponding to the C-H and C-C-O of hydrocarbon and C-O of $(\text{RCOCO}_2)^-$ were observed²². Meanwhile, a high oxidation state of 293.8 eV , which has rarely been reported for LIBs, was also observed. This peak could be assigned to the C-F binding state, probably because of the electrolyte salt participant reduction process on the Sn anode. As for the Ca 2p and F 1s spectra (Supplementary Fig. 4b,c), binding energies corresponding to CaF_2 and $\text{Ca}(\text{PF}_6)_2$ were observed, suggesting that inorganic compound CaF_2 is also one of the solid electrolyte interface (SEI) components². In the O 1s spectra (Supplementary Fig. 4d), two peaks located at 532.2 and 534.0 eV were observed, corresponding to $(\text{ROCO}_2)^-$ and $(\text{ROCO}_2)^-$, respectively. Notably, no signals belonging to CaO were observed, suggesting that CaO is not the SEI component.

To ascertain whether the alloying of Ca ions occurred uniformly, we further characterized the morphology and elemental distribution of the Sn anode before and after battery reactions (Fig. 1g,h and Supplementary Fig. 5). The initial Sn shows a smooth surface with an obvious metallic luster (Fig. 1g), and its colour changes to

dark grey with a thin alloy layer about 500 nm thick after 300 cycles (Fig. 1h and inset). This is consistent with the elemental maps of the charged Sn anode that show Ca and Sn homogeneously distributed on the anode surface (Supplementary Fig. 5). C, O and F were also observed on the charged Sn anode, in accordance with the XPS spectra. Furthermore, no dendrites formed on the Sn anode even after 300 cycles (Fig. 1h), indicating the high stability of using Sn as the alloying anode in this novel CIB.

We also carried out XRD of the Sn anode during the first cycle for different charged states. Nine states, indicated by coloured circles in Fig. 2a, were selected, and their XRD patterns are shown in Fig. 2b,c. In the initial stage, pure Sn was observed with obvious diffraction peaks corresponding to tetragonal Sn (JCPDS # 01-089-2958). When the Sn anode was gradually charged to 4.0 V, a diffraction peak at 22.8° was observed (Fig. 2b) which could be attributed to the (201) peak of Ca_7Sn_6 . As charging continued, a larger amount of Ca_7Sn_6 formed and the intensity of the peak increased correspondingly (Fig. 2c). At the fully charged state (5.0 V), the intensity reached its highest value and then decreased gradually as discharging proceeded. The small residual peak at the fully discharged state at 3.0 V indicates non-ideal reversibility due to the kinetic limitations of the solid state electrochemical reactions²³. It is worth noting that only one diffraction peak was observed for Ca_7Sn_6 during the first cycle, compared to eight dominant peaks after 300 cycles (Fig. 1f); these are attributed to the shallow intercalation of Ca in the Sn during the initial cycle. Figure 2d shows the crystal structure of Ca_7Sn_6 resulting from electrochemical alloying between Ca ions and the Sn anode. During charging, Ca ions diffuse into the Sn lattice and bond with Sn atoms in four different situations: two types of Ca are surrounded by six nearest Sn atoms, forming a distorted octahedron (P1 and P2 in Fig. 2d); the other two types are surrounded by seven nearest Sn atoms, forming a distorted decahedron (P3 and P4 in Fig. 2d). We calculated the formation energies for P1–P4 (Supplementary Fig. 6), which are all negative in the order $\text{P1} > \text{P2} > \text{P3} > \text{P4}$, in agreement with the successful alloying/de-alloying process between the Sn anode and Ca. During discharge, de-alloying causes Ca_7Sn_6 to transform back to pristine Sn (space group of $I4_1/amd$). This reversible alloying/de-alloying process enables the Sn anode to provide a high capacity of 526 mAh g^{-1} with a volume expansion of 136.8%.

Internal stress due to volume expansion is critical for the mechanical reversibility and structural stability of a metal anode. To monitor the stress evolution of the Sn anode during battery reactions, we carried out in situ stress measurements during the first cycle (see Methods for experimental details). The film electrode was assembled into an electrochemical cell with natural graphite as the cathode (Supplementary Fig. 7a). The in situ stress was measured (Supplementary Fig. 7b,c) by the cantilever beam-bending method based on the Stoney equation²⁴,

$$\sigma = \frac{E_s h_s^2}{6(1-\nu_s)h_f} \times \left(\frac{1}{R_t} - \frac{1}{R_0} \right) \quad (1)$$

where E , ν and h are Young's modulus, Poisson's ratio and the thickness, respectively. Subscripts s and f indicate the substrate and film, respectively, R_0 is the initial curvature radius, and R_t is the curvature radius at any charge or discharge state. Stress evolution during the first cycle was monitored and plotted against voltage in Fig. 2e. During charging, compressive stress builds as Ca–Sn alloying proceeds, increasing slowly up to 4.34 V , and then more rapidly until reaching -48.13 MPa . During discharge, the compressive stress gradually decreases as the Ca–Sn de-alloys. Stress is dominant in the voltage range $3.5\text{--}5.0\text{ V}$ (the shaded area in Fig. 3e), and this is consistent with the charge/discharge voltage plateaux of the CIB. During the entire charge/discharge cycle, the

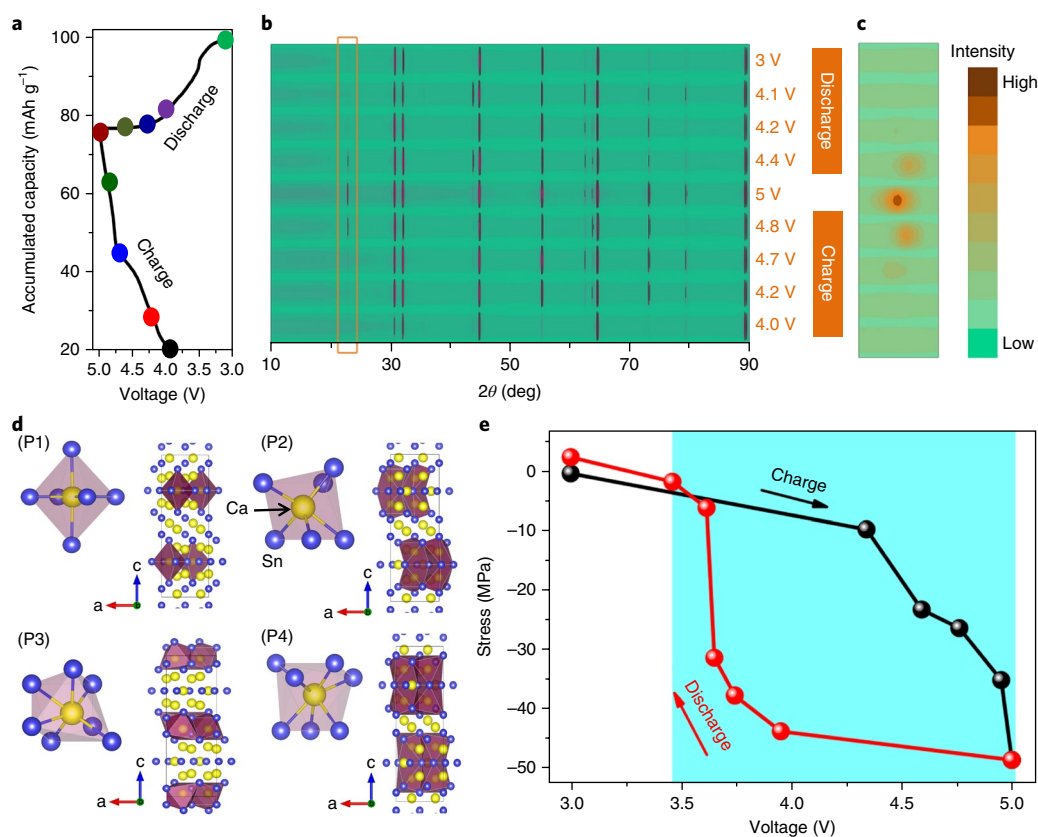


Fig. 2 | Electrochemical and mechanical reversibility of the Sn anode. **a**, Typical galvanostatic charge-discharge profile of a CIB. **b**, XRD profiles of a Sn anode cycled to different charge states, as marked by the coloured circles in **a**. **c**, Detailed view of the boxed area in **b** showing the XRD patterns of a Sn anode from 22° to 24°. The intensity change indicates variation in the amount of Ca₇Sn₆ alloy versus the charge states. **d**, Four different bonding situations for Ca and Sn in the Ca₇Sn₆ alloy. Yellow and blue balls represent Ca and Sn atoms, respectively. **e**, In situ stress measurement of a Sn anode during charge-discharge during the first cycle. The shaded area indicates the stress-dominant area.

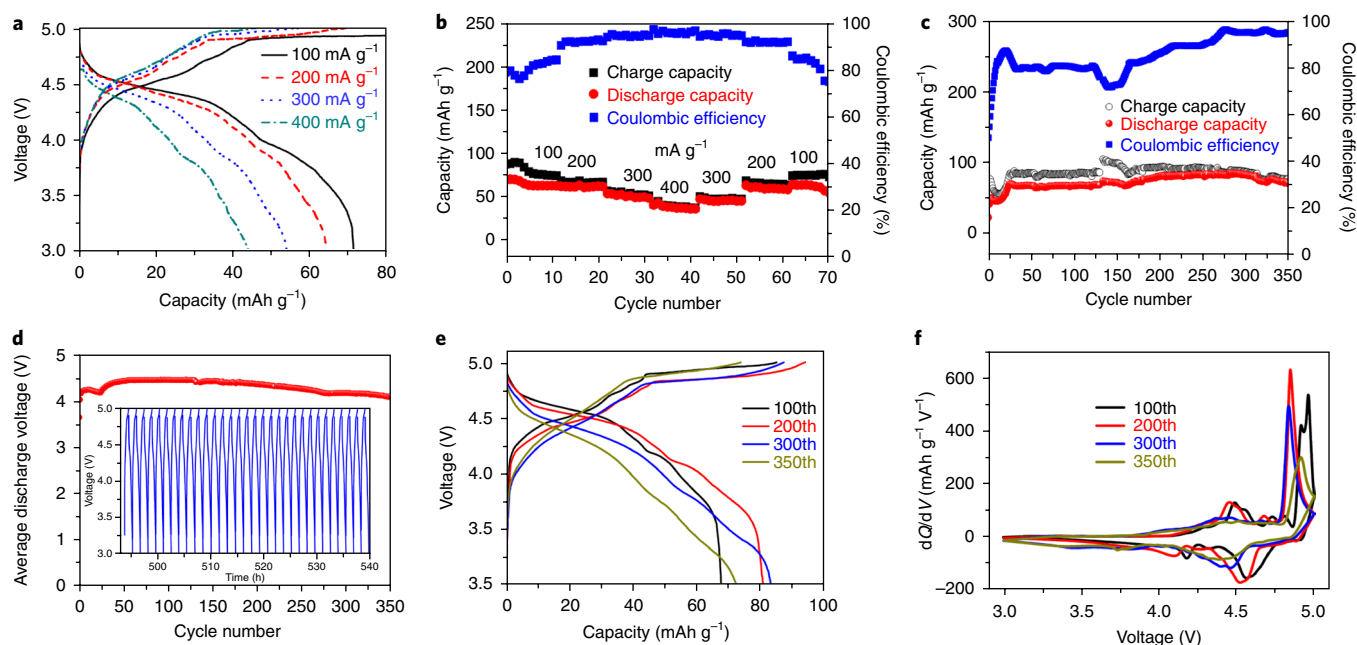


Fig. 3 | Electrochemical performance of a CIB. **a**, Charge-discharge performance of a CIB at different current densities ranging from 100 to 400 mA g⁻¹. **b**, Charge-discharge capacities and corresponding coulombic efficiencies of a CIB at different current densities. **c**, Cycling stability of a CIB. **d**, Average discharge voltage of a CIB during 350 cycles. Inset: Average discharge voltage for the final 30 cycles. **e**, Galvanostatic charge-discharge profiles of a CIB at the 100th, 200th, 300th and 350th cycles. **f**, dQ/dV plots of a CIB at the 100th, 200th, 300th and 350th cycles.

Sn anode is usually in compression, which is helpful to inhibit the initiation and propagation of cracks²⁵, thus enhancing the structural stability of the Sn anode and making the alloying/de-alloying highly reversible. Better mechanical reversibility is expected by introducing nanoscale or amorphous Sn-based anode materials²⁶, as such structures can release the volume change of the Sn anode during battery cycling.

Figure 3a shows the galvanostatic charge–discharge curves of the CIB with different current densities ranging from 100 to 400 mA g^{−1} over a potential window of 3.0–5.0 V. The CIB exhibited good capacity retention at high rates, indicating low electrode polarization. Figure 3b shows the rate capacities of the CIB, accompanied by the corresponding coulombic efficiencies. Discharge capacities of 72, 64, 53 and 40 mAh g^{−1} were achieved at 100, 200, 300 and 400 mA g^{−1}, respectively. The discharge capacities return to their initial values when the discharge current decreases, suggesting the good reversibility of the CIB. We also performed long-term cycling stability measurements of the CIB at 100 mA g^{−1} for 350 cycles (Fig. 3c). For the first few cycles, the discharge capacity of the CIB was about 50 mAh g^{−1}, then it gradually increased to 85 mAh g^{−1} at the 200th cycle. As the electrochemical reaction proceeded, a larger amount of Ca₇Sn₆ formed and participated in the reversible alloying/de-alloying reaction, leading to the capacity increase (Supplementary Fig. 8). Furthermore, the impedance decreased with number of cycles (Supplementary Fig. 9), indicating that the gradually increasing diffusion efficiency might be another reason for the capacity increase. Even after 350 cycles, 95% of the capacity obtained for the 200th cycle was retained, demonstrating the high stability of the Ca-based electrochemistry in this novel battery configuration. The coulombic efficiencies of the CIB are also relatively high at between 80 and 95%, with few exceptions.

Figure 3d shows the average discharge voltage (working voltage) of the CIB for 350 cycles, with the charge–discharge profiles for the last 30 cycles shown in the inset. The entire test lasted 540 h. At the beginning of the measurement, the CIB had an average discharge value of 4.2 V, which gradually increased to 4.45 V and then gradually decreased. Even after 350 cycles, the CIB can still achieve an average discharge voltage of 4.08 V, which is much higher than previously reported CIBs and even higher than most LIBs. Moreover, the proposed CIB achieved an energy efficiency of around 80% after activation, which is higher than the molten Ca–Mg alloy|Bi battery (~70%)¹⁰, and comparable with the nickel hexacyanoferrate|activated carbon battery (~83%)⁵. Figure 3e shows the charge–discharge profiles of the CIBs at the 100th, 200th, 300th and 350th cycles, demonstrating stable battery performance with small electrode polarization. Figure 3f shows the corresponding dQ/dV curves. In the charge process, the onset potentials and anion intercalation peaks shifted to lower values for the 200th and 300th cycles, suggesting gradually improved reaction kinetics¹⁶. The shift of the main peak towards a higher potential and the decrease of the intensity for the 350th cycle indicated that the staging effects of anions' intercalation/de-intercalation into graphite became less dominant²⁷. Meanwhile, the gradual shift of the dominant peaks towards lower potentials during the discharge process indicates that slight polarization is occurring as the cycling number increases. Although the electrochemical performance of this CIB may be further improved by optimizing the electrolyte systems and surface structures of the Sn anode and using novel layered cathode materials, and so on, the results presented here clearly indicate the feasibility of CIBs operating at room temperature. We also believe that new configuration strategies can widen the selection of active materials (for example, for anodes, cathodes and electrolytes) and extend the range of CIB systems, which may be helpful in achieving ideal performance for energy storage applications.

Methods

Materials. Al foil (thickness, ~20 µm), Zn foil (thickness, ~100 µm), Li foil (thickness, ~100 µm), Na foil (thickness, ~50 µm), natural graphite powder, polyvinylidene fluoride (PVDF) binder, conductive carbon black and *N*-methyl-2-pyrrolidone (NMP) were purchased from Shenzhen KejingStar Technology. Ca(PF₆)₂, EC, PC, EMC and DMC were purchased from Suzhou Qianmin Chemical Reagent Co. The glass fibre separator (Whatman, 47 mm) was purchased from Shanghai Huanao Technology. All chemicals were used directly as purchased without further processing.

Characterization. Scanning electron microscope (SEM) measurements were carried out on a Hitachi S-4800 equipped with an energy dispersive X-ray (EDX) detector. XRD patterns were obtained on a Rigaku Miniflex 600 diffractometer operated at 40 kV and 15 mA (Cu Kα radiation). The chemical composition was characterized by XPS (ESCALAB 250Xi, Thermo Fisher) using monochromatic aluminium Kα radiation. Raman spectra were recorded on a LabRAM HR Raman spectrometer (532 nm). After cycling, all samples were thoroughly cleaned with EMC before SEM, Raman, XPS and XRD measurements.

Electrochemical characterization. A mixture of natural graphite, PVDF and conductive acetylene black in weight ratios of (8:1:1) was ground thoroughly and a certain amount of NMP was then added to form a homogeneous slurry. The slurry was coated onto an Al foil and dried at 80 °C in a vacuum oven for 12 h for use as the cathode. The graphite cathode, a Sn anode and a glass fibre separator were punched into circular sheets with diameters of 10, 12 and 16 mm, respectively. Ca(PF₆)₂ (0.8 M) in different carbonate solvents as the electrolyte was prepared in an argon-filled glove box (Etelux Lab2000) with both water and oxygen contents less than 0.1 ppm. The cathode, anode, glass fibre separator and electrolyte were then assembled into a CR2032 coin-type cell in the glove box. The areal surface density of the active material on the Al current collector was ~2 mg cm^{−2}, and the amount of electrolyte used in one coin-cell was ~0.2 ml. All galvanostatic charge–discharge measurements were carried out on a battery test system (LAND CT2001A) at room temperature. Electrochemical impedance spectroscopy (EIS) measurements were performed on an Autolab (PGSTAT302N) electrochemical workstation. All gravimetric capacities were calculated based on the weight of cathode material.

In situ stress test. Sn film electrodes were fabricated by depositing Sn on the unpolished side of 304 stainless-steel strip substrate (50 mm × 10 mm × 0.8 mm) by d.c. magnetron sputtering (DSC 250 Coater, Shenzhen SuPro Instruments). A Sn disc (2 inch diameter, 99.95% purity) was used as the target, with a target power of 20 W. The pressure was set to 0.5 Pa with Ar (99.995%) as the working gas. Note that the other side of the steel strip was mirror-polished to reflect the laser beam. Before deposition, the substrates were ultrasonically cleaned in ethanol and acetone and then dried with N₂. The deposition time was controlled to deposit a Sn film with a thickness of 2 µm.

The electrochemical cell is illustrated in Supplementary Fig. 7a. An Al foil (50 mm × 10 mm × 20 µm) coated with natural graphite was used as the cathode. The cathode was placed beneath the Sn film anode, face to face, at a distance of ~3 mm. Cell assembly was carried out in an argon-filled glove box with water and oxygen contents below 0.1 ppm.

The in situ stress test set-up was built in house as illustrated in Supplementary Fig. 7b (for a photograph see Supplementary Fig. 7c). A He–Ne laser source (Thorlabs, HNL050L) was used to produce the laser beam, which passed through a translucent mirror into the electrochemical cell and was then reflected first by the electrolyte/substrate interface and then the translucent mirror. The reflected laser beam finally fell on a charge-coupled device (CCD) camera, which was sensitive to the laser spot position associated with bending of the electrode. When the anode sample moved a distance Δ*L*, the corresponding distance change of the laser spot on the camera was Δ*D*. The radius of curvature of the steel strip *R* was calculated by the formula

$$R = 2(H_1 + H_2) \cdot \frac{1}{\Delta D / \Delta L} \quad (2)$$

where *H*₁ and *H*₂ are the respective distances from the substrate to the translucent mirror and from the mirror to the CCD camera. Δ*D* and Δ*L* are, respectively, the distances that the anode sample and the laser spot move. The radius of curvature of the steel strip changes with time during the charge/discharge process. Electrochemical measurements were conducted using the battery test system LAND CT2001A at a current rate of 0.5 C from 3 V to 5 V. Stress data were recorded during the charging and discharging processes.

Data availability. The data supporting the findings of this work are available within the Article and its Supplementary Information, or from the corresponding author upon reasonable request.

Received: 26 November 2017; Accepted: 13 March 2018;

Published online: 23 April 2018

References

- Lin, M.-C. et al. An ultrafast rechargeable aluminium-ion battery. *Nature* **520**, 324–328 (2015).
- Ponrouch, A., Frontera, C., Bardé, F. & Palacin, M. Towards a calcium-based rechargeable battery. *Nat. Mater.* **15**, 169–173 (2016).
- Larcher, D. & Tarascon, J.-M. Towards greener and more sustainable batteries for electrical energy storage. *Nat. Chem.* **7**, 19–29 (2015).
- Shterenberg, I., Salama, M., Gofer, Y., Levi, E. & Aurbach, D. The challenge of developing rechargeable magnesium batteries. *MRS Bull.* **39**, 453–460 (2014).
- Wang, R. Y., Wessells, C. D., Huggins, R. A. & Cui, Y. Highly reversible open framework nanoscale electrodes for divalent ion batteries. *Nano Lett.* **13**, 5748–5752 (2013).
- Wang, R. Y. et al. Reversible multivalent (monovalent, divalent, trivalent) ion insertion in open framework materials. *Adv. Energy Mater.* **5**, 1401869 (2015).
- Arroyo-de Dompablo, M. E. et al. A joint computational and experimental evaluation of CaMn_2O_4 polymorphs as cathode materials for Ca ion batteries. *Chem. Mater.* **28**, 6886–6893 (2016).
- Lipson, A. L. et al. Rechargeable Ca-ion batteries: a new energy storage system. *Chem. Mater.* **27**, 8442–8447 (2015).
- Aurbach, D., Skaletsky, R. & Gofer, Y. The electrochemical behavior of calcium electrodes in a few organic electrolytes. *J. Electrochem. Soc.* **138**, 3536–3545 (1991).
- Ouchi, T., Kim, H., Spatocco, B. L. & Sadoway, D. R. Calcium-based multi-element chemistry for grid-scale electrochemical energy storage. *Nat. Commun.* **7**, 10999 (2016).
- Gogotsi, Y. & Simon, P. True performance metrics in electrochemical energy storage. *Science* **334**, 917–918 (2011).
- Simon, P. & Gogotsi, Y. Materials for electrochemical capacitors. *Nat. Mater.* **7**, 845–854 (2008).
- Bai, S. Y., Liu, X. Z., Zhu, K., Wu, S. C. & Zhou, H. S. Metal–organic framework-based separator for lithium-sulfur batteries. *Nat. Energy* **1**, 16094 (2016).
- Kim, J. H. et al. Stabilization of insoluble discharge products by facile aniline modification for high performance Li–S batteries. *Adv. Energy Mater.* **5**, 1500268 (2015).
- Seel, J. & Dahn, J. Electrochemical intercalation of PF_6^- into graphite. *J. Electrochem. Soc.* **147**, 892–898 (2000).
- Placke, T. et al. Influence of graphite characteristics on the electrochemical intercalation of bis(trifluoromethanesulfonyl) imide anions into a graphite-based cathode. *J. Electrochem. Soc.* **160**, A1979–A1991 (2013).
- Xu, K. Nonaqueous liquid electrolytes for lithium-based rechargeable batteries. *Chem. Rev.* **104**, 4303–4418 (2004).
- Sheng, M., Zhang, F., Ji, B., Tong, X. & Tang, Y. A novel tin-graphite dual-ion battery based on sodium-ion electrolyte with high energy density. *Adv. Energy Mater.* **7**, 1601963 (2017).
- Lee, Y., Lee, J., Kim, H., Kang, K. & Choi, N.-S. Highly stable linear carbonate-containing electrolytes with fluoroethylene carbonate for high-performance cathodes in sodium-ion batteries. *J. Power Sources* **320**, 49–58 (2016).
- Fan, H., Qi, L. & Wang, H. Hexafluorophosphate anion intercalation into graphite electrode from methyl propionate. *Solid State Ion.* **300**, 169–174 (2017).
- Jain, A. et al. Commentary: The Materials Project. A materials genome approach to accelerating materials innovation. *Appl. Mater.* **1**, 011002 (2013).
- Schechter, A., Aurbach, D. & Cohen, H. X-ray photoelectron spectroscopy study of surface films formed on Li electrodes freshly prepared in alkyl carbonate solutions. *Langmuir* **15**, 3334–3342 (1999).
- Borg, R. & Dienes, G. J. *An Introduction to Solid State Diffusion* (Academic, San Diego, 1988).
- Stoney, G. G. The tension of metallic films deposited by electrolysis. *Proc. R. Soc. Lond.* **82**, 40–43 (1909).
- Zhang, S. *Nanostructured Thin Films and Coatings: Mechanical Properties 1* (CRC, Boca Raton, 2010).
- Fang, L. & Chowdari, B. Sn–Ca amorphous alloy as anode for lithium ion battery. *J. Power Sources* **97**, 181–184 (2001).
- Noel, M. & Santhanam, R. Electrochemistry of graphite intercalation compounds. *J. Power Sources* **72**, 53–65 (1998).

Acknowledgements

The authors thank Nanzhong Wu and Lei Shi for data analysis and in situ stress measurements. The authors acknowledge financial support from the National Natural Science Foundation of China (grant no. 51302238), Shenzhen Peacock Plan (KQJSCX20170331161244761 and KQTD2016112915051055), the Natural Science Foundation of Guangdong Province (no. 2017A030310482), Shenzhen Science and Technology Planning Project (JCYJ20160122143155757, JSGG20160301173854530, JSGG20160301155933051, JSGG20160229202951528, JCYJ20170307171232348, JCYJ20170307172850024 and JSGG20170413153302942), Guangdong Engineering Technology Research Center Foundation (no. 20151487), Shenzhen Engineering Laboratory Foundation (no. 20151837), and the Scientific Equipment Project of the Chinese Academy of Sciences (GJHS20170314161200165, yz201440).

Author contributions

Y.B.T. and H.-M.C. conceived and designed the experiments. M.W. and S.Q.Z. performed electrochemical experiments. C.L.J. conducted in situ stress measurements. M.W. and S.Q.Z. conducted XRD, Raman, XPS and SEM measurements. X.H.S. conducted simulation work. Y.B.T., M.W., C.L.J., X.H.S. and H.-M.C. co-wrote the paper. All authors discussed the results and commented on the manuscript.

Competing interests

The authors declare no competing interests.

Additional information

Supplementary information is available for this paper at <https://doi.org/10.1038/s41557-018-0045-4>.

Reprints and permissions information is available at www.nature.com/reprints.

Correspondence and requests for materials should be addressed to Y.T. or H.-M.C.

Publisher's note: Springer Nature remains neutral with regard to jurisdictional claims in published maps and institutional affiliations.